Remotely Sensing the Earth's Atmosphere Using the Global Positioning System (GPS)—The GPS/MET Data Analysis

DEREK D. FENG AND BENJAMIN M. HERMAN

Institute of Atmospheric Physics, The University of Arizona, Tucson, Arizona

(Manuscript received 31 July 1998, in final form 5 October 1998)

ABSTRACT

The Global Positioning System/Meteorology (GPS/MET) project is an active satellite-to-satellite remote sensing experiment using the radio occultation technique. Due to the atmospheric index of refraction and gradient of the index of refraction, GPS signals propagate through the earth's atmosphere along a slightly curved path and with slightly retarded speeds. When these signals arrive at a receiver aboard a low earth orbit satellite, the receiver records an excess phase delay compared with the phase delay of a straight line propagation in a vacuum. Using the Abel integral equations, the phase delay rates with time can be converted into the atmospheric index of refraction profile; then, using the hydrostatic equation, the pressure and temperature profiles may be derived.

This paper describes the principles of the GPS/MET occultation experiment and the detailed data analysis procedure. Data smoothing technique and error analysis are also discussed. Some GPS/MET intermediate and final retrieval results, such as ray bending angle and temperature and pressure profiles, are presented for illustration. Although random noise in the GPS/MET measurements leads to an uncertainty of ~0.1–0.3 K in the retrieved temperatures, comparisons of the GPS/MET retrieval results with radiosonde measurements, other remote sensing observations, and numerical analyses show that without the multipath corrections the GPS/MET temperature profiles accurate to within 1°–2°C can be obtained from ~5–7 to ~40 km above the ground. Despite the fact that a few outstanding problems in the GPS/MET data retrievals remain to be addressed, overall the GPS/MET occultation method has been demonstrated to be capable of producing accurate, all-weather, round-the-clock, global refractive index, density, pressure, and temperature profiles of the troposphere and stratosphere.

1. Introduction

The Global Positioning System/Meteorology project, hereinafter called GPS/MET, is a proof-of-concept microwave occultation experiment. It is intended to demonstrate that remotely sensing the earth's atmosphere by means of radio occultation using the GPS is feasible, reliable, and relatively inexpensive. Since mid-1995, this project has produced, with more than acceptable accuracy, many thousands of refractive index, temperature, density, and pressure profiles of the atmosphere, distributed over both land and ocean areas, from 1 to 40 km or more (Ware et al. 1996; Kursinski et al. 1996, 1997; Rocken et al. 1997).

Studies of planetary atmospheres using radio occultation are by no means new. In fact, radio occultation has been used in probing planetary atmospheres for more than three decades (Eshleman 1973; Tyler 1987). The Jet Propulsion Laboratory (JPL) and Stanford University's radio astronomy group first developed the microwave occultation technique for studying planetary atmospheres. Since then, radio occultation has played a major role in many United States solar system exploration missions, such as Pioneer, Mariner, Voyager, and Magellan. In conjunction with other observation methods, radio occultation techniques have revealed considerable knowledge about temperatures, pressures, and composition of the atmospheres of the inner planet Venus (Fjeldbo et al. 1971; Lipa and Tyler 1979; Steffes et al. 1994; Jenkins and Steffes 1994; Hinson and Jenkins 1995) and the outer planets (Kliore et al. 1965; Fjeldbo and Eshleman 1968; Lindal et al. 1979, 1981, 1983, 1985, 1987; Lindal 1992). Some of the planetary satellites and ring systems have also been studied by radio occultation techniques (Marouf et al. 1982; Tyler et al. 1983, 1989; Lindal et al. 1983).

Although scientists have long recognized the usefulness of radio occultation in studies of planetary atmospheres, this technique had not been employed in probing the earth's atmosphere until the GPS/MET project. The first proposal to utilize the GPS satellites for the earth's atmosphere studies came from JPL in 1988. Four

Corresponding author address: Derek D. Feng, Institute of Atmospheric Physics, The University of Arizona, P.O. Box 210081, Tucson, AZ 85721-0081.
E-mail: feng@air.atmo.arizona

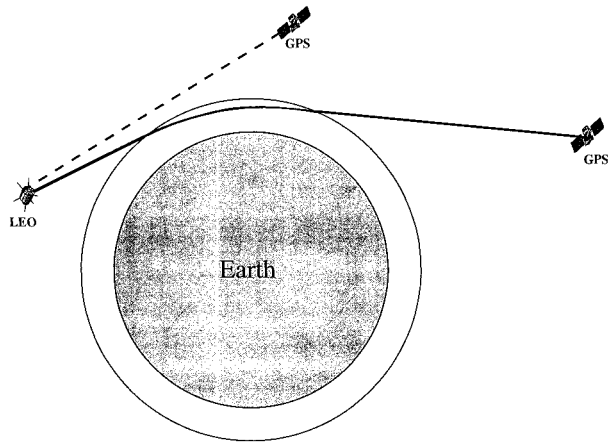

FIG. 1. GPS/MET occultation experiment. An occultation is taking place between the LEO and the GPS connected with the solid line. Note that the solid line is slightly curved in the atmosphere.

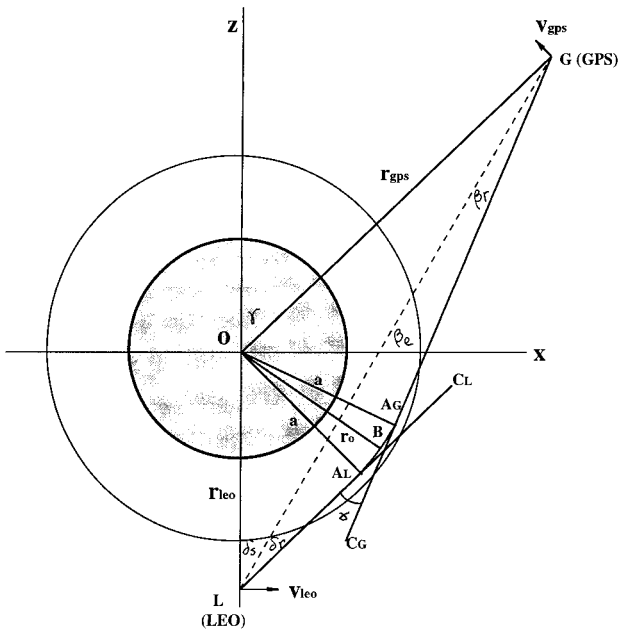

FIG. 2. GPS/MET Occultation Geometry. The figure plane is the occultation plane.

years later when the GPS was already fully operational, in a short article, Ware (1992) suggested limb sounding the earth's atmosphere by using the GPS. With financial support from the National Science Foundation, the National Oceanic and Atmospheric Administration, the Federal Aviation Administration, and the National Aeronautical and Space Administration, the GPS/MET project started in the summer of 1993. On 3 April 1995, a small research satellite, *MicroLab-1,* was successfully put into a low earth orbit (LEO). A GPS receiver developed by JPL was on board. The following ~2 years served to validate the GPS radio occultation method.

GPS/MET is an active satellite-to-satellite remote sensing experiment using the occultation technique. It differs from most other satellite remote sensing methods in that it is an active probe and uses measurements of phase, rather than intensity. Furthermore, the GPS signals are regulated by atomic clocks, which means the GPS occultation measurements do not need additional calibration. These features make the GPS/MET a new and precise sounding technique for the earth's atmosphere. The technique enables us to produce accurate, all-weather, round-the-clock, global refractive index, density, pressure, and temperature profiles of the troposphere and stratosphere and electron density profiles of the ionosphere. Therefore the GPS/MET technique has the potential to improve weather analyses, to monitor climate change, and to provide ionospheric data at comparatively low cost.

Ware et al. (1996), Kursinski et al. (1996, 1997), and Rocken et al. (1997) presented the detailed preliminary results and statistical validation of the GPS/MET experiment. The current paper will present the principles of the earth radio occultation experiment and details of the data analysis procedure conducted at The University of Arizona. To illustrate, some retrieval results will also be presented.

2. Principles and formulation of the GPS/MET microwave occultation experiment

The GPS was developed by the Department of Defense primarily for military uses. It consists of 24 GPS satellites that are evenly distributed in the space around the earth. Each of these satellites transmits two coded signals at carrier frequencies 1.575 42 GHz (carrier L1) and 1.227 60 GHz (carrier L2) (Hofmann-Wellenhof et al. 1997). The GPS/MET receiver is on board the low earth orbiting *MicroLab-1* (i.e., the LEO). If the relative positions and motions among the GPS, the LEO, and the earth are proper, the radio ray path between the GPS and LEO passes through the earth's atmosphere, and occultation occurs.

Figure 1 illustrates the GPS/MET occultation experiment, where the outer annulus represents the atmosphere of the earth. In the figure, an occultation is occurring between the LEO and the GPS satellites connected by a solid line. With the current configuration of 24 GPS transmitters, approximately 500 GPS/MET occultations per day could take place for each LEO.

A fundamental assumption in the GPS/MET occultation is that the earth's atmosphere is spherically symmetric. That implies that all atmospheric parameters, such as temperature, pressure, density, and refractive index, are functions of radius only. Figure 2 shows the GPS/MET occultation geometry. The inner circle is the earth; the outer annulus represents the atmosphere. The center of the earth is at the origin, O, of the coordinates. Here, G and L denote the GPS and the LEO, respectively. The gradient of the atmospheric density leads to the refractive index gradient. The radio ray transmitted from the GPS propagates through the atmosphere and arrives at the

LEO along a slightly curved path ($G–A_G–B–A_L–L$) due to the index gradient. Because rays bend toward the region of higher refractive index, they almost always bend downward in the neutral part of the atmosphere and may bend either up or down in the ionosphere. This paper is mainly concerned with the neutral atmosphere; therefore the ray path illustrated in Fig. 2 is shown bending downward toward the earth. Here, GC_G and LC_L are the two ray asymptotes for radio ray $G–A_G–B–A_L–L$. The angle between two asymptotes, α, is the bending angle, while the perpendicular distance from the center of the earth to the two asymptotes is the impact distance a. Because of the spherically symmetric assumption for the atmosphere, the impact distances to each asymptote are equal. Here, B is the perigee, the point along the radio path that is the shortest radial distance from the earth; $r_0 = OB$ denotes that radial distance. In the ingress (egress) occultation, α increases (decreases) as the ray path gradually immerses into (emerges from) the denser atmosphere. Thus, the bending angle α is numerically a function of impact distance a: $\alpha = \alpha(a)$. For the earth's atmosphere, the maximum bending angle is $\sim 1.5°$ at the ground level and may be as small as $\sim 10^{-4}$ degree at 60-km height. Such a small angle cannot be directly measured. Instead, in the GPS/MET occultation, the carrier phases are measured. By calculating the time derivative of the phases, a frequency different from the nominal L1 or L2 frequency and known as the Doppler-shifted frequency f_d, may be obtained.

In Fig. 2, the GPS and LEO satellites and the center of the earth form the occultation plane. The LEO satellite is located on the negative z axis with OL equal to its orbiting radius, r_{LEO}, around the earth. Here, OG is the GPS orbiting radius r_{GPS}. Note that two satellites and the earth constitute an occultation plane at every occultation epoch, but the velocity vectors of the GPS and the LEO are not coplanar. The velocity components of the GPS and LEO normal to the occultation plane do not contribute to the Doppler-shifted frequencies. With the two impact distances on the LEO and GPS side being equal, the Doppler-shifted frequencies combined with the satellite ephemerides can be used to uniquely determine the impact distance a and the bending angle α at every occultation epoch.

For the spherically stratified atmosphere, the Abel integral equation gives a relationship between bending angle $\alpha(a)$ and refractive index $\mu(a)$ (Phinney and Anderson 1968; Fjeldbo et al. 1971):

$$\mu(a_0) = \exp\left\{\frac{1}{\pi} \times \int_{a_0}^{\infty} \frac{\alpha(a)\, da}{(a^2 - a_0^2)^{1/2}}\right\}, \qquad (2.1)$$

where $a_0 = \mu(a_0)r_0 = \mu(r_0)r_0$ (r_0 is the radial distance from the center of the earth to the radio path at the perigee point B). Thus, once the numerical function $\alpha(a)$ is calculated from the Doppler-shifted frequencies, Eq. (2.1) yields the reflective index μ at a_0 or r_0. By varying a_0, we can obtain index profile $\mu(a_0)$ or $\mu(r_0)$.

Refractive index μ is a physical property of the medium. For the earth's neutral atmosphere and for the radio frequencies below 20 GHz, index μ may be related to the dry air pressure P_d in millibars, temperature T in Kelvins, and water vapor partial pressure E also in millibars by the expression (Liebe 1989):

$$(\mu - 1) \times 10^6 = 0.2588P_d(300/T) + [4.163(300/T) + 0.239]E(300/T). \qquad (2.2)$$

If we define the atmospheric refractivity N as

$$N = (\mu - 1) \times 10^6, \qquad (2.3)$$

then, with sufficient accuracy, Eq. (2.2) may be rewritten as (Smith and Weintraub 1953; Thayer 1974)

$$N = 77.6\frac{P}{T} + (3.73 \times 10^5)\frac{E}{T^2}, \qquad (2.4)$$

where temperature T is in Kelvins and water vapor pressure E is in millibars. Here, P in Eq. (2.4) is the total atmospheric pressure in millibars. When the water vapor contribution may be neglected (say, at higher altitude where $E \cong 0$), then

$$N = 77.6\frac{P}{T} = 77.6\rho R, \qquad (2.5)$$

where ρ is the atmospheric density and R is the specific gas constant.

The temperatures derived from Eqs. (2.4) and (2.5) are referred to as the wet (true) and dry temperatures, respectively. Obviously, without the help of additional independent information about the atmosphere, Eq. (2.4) may not be solved, as there are three unknowns for each retrieved value of N. However, above the middle troposphere (say, above ~ 7 km from the ground), where little water vapor exists, we may ignore the water vapor term in Eq. (2.4). Equation (2.5) would then be a good approximation to the real atmosphere, and the vertical density profile $\rho(z)$ can be solved for.

Combining Eq. (2.5) with the hydrostatic equation $dP = -g\rho\, dz$ and the equation of state $P = \rho RT$ yields an expression for the pressure profile $P(z)$,

$$P(z) = \int_z^{\infty} g(z')\rho(z')\, dz' = \frac{1}{77.6R}\int_z^{\infty} N(z')g(z')\, dz' = \frac{1}{77.6\text{R}}\int_z^{z_{\text{top}}} N(z')g(z')\, dz' + P(z_{\text{top}}), \qquad (2.6)$$

and the temperature profile $T(z)$ is then given by

$$T(z) = 77.6\frac{P(z)}{N(z)} = \frac{1}{RN(z)}\int_z^{\infty} g(z')N(z')\, dz' = \frac{1}{RN(z)}\int_z^{z_{\text{top}}} g(z')N(z')\, dz' + \frac{77.6}{N(z)}P(z_{\text{top}}), \qquad (2.7)$$

where $g(z)$ is the gravitational acceleration, R is the

specific gas constant, and z is the altitude. The $P(z_{top})$ in Eqs. (2.6) and (2.7) is the boundary value of the pressure at the altitude z_{top}, the uppermost altitude where the value of N is available.

Temperature derived in the above manner is called the ''dry'' temperature because the water vapor pressure E in Eq. (2.4) has been set to zero (dry atmosphere). This is generally a good working assumption for atmospheric altitudes higher than ~5–7 km where E is negligible. To the contrary, in the lowest part of the troposphere, particularly in the low-latitude regions where water vapor is usually plentiful, these dry temperatures substantially differ from the actual atmospheric temperatures, causing larger cold bias in the retrieved GPS/MET temperatures. The more water vapor in the atmosphere, the colder the GPS/MET dry temperature would be.

Although this cold bias of temperatures may cause some inconvenience or confusion, it is actually an opportunity to recover the much-needed water vapor profiles. When reasonably accurate independent temperature and/or pressure information is available from the National Centers for Environmental Prediction or the European Centre for Medium-Range Weather Forecasting analyses, water vapor distribution in the lower troposphere may be recovered using the GPS/MET refractivity N, since the water vapor effect is fully integrated in N (Kursinski et al. 1995; Rocken et al. 1997).

3. GPS/MET occultation data retrieval and error analysis

a. Data retrieval

GPS/MET data retrieval involves implementation of the occultation principles and formulas described in section 2. The output of the retrieval consists of the refractivity profile $N(z)$, temperature profile $T(z)$, and pressure profile $P(z)$, where z is the altitude above the mean sea level at the occultation location. In this section, we shall describe some major steps in the retrieval process. Figure 3 shows the flowchart of the GPS/MET occultation data retrieval, covering the major steps in converting the occultation observables, the L1 and L2 phase data, to the N, T, and P profiles.

1) PHASE DATA AND DOPPLER-SHIFTED FREQUENCIES

During a GPS/MET occultation, the phases $\phi(t)$ of carrier L1 (1.575 42 Ghz, $\lambda = 19.03$ cm) and carrier L2 (1.227 60 Ghz, $\lambda = 24.42$ cm) as functions of time t are measured and recorded. The data sampling rate is set to 50 Hz. The derivative of the phase with respect to time yields the Doppler-shifted frequency, that is, $f_d = (\Delta\phi)/(\Delta t)$. We have two sets of f_d's, one for L1 and the other for L2. The raw Doppler-shifted frequency data are noisy and require some type of smoothing before being fed into the next data analysis step.

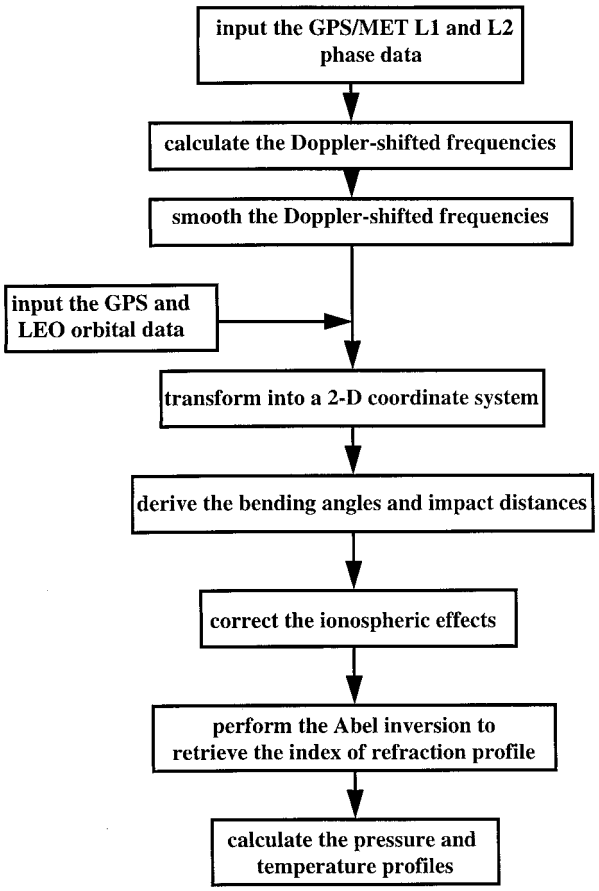

FIG. 3. GPS/MET data analysis flowchart.

2) DATA SMOOTHING

The Abel Eq. (2.1) requires an integration from a_0 to infinity. A requirement inherent in the Abel integration is that impact distance a must never be less than parameter a_0. A violation of this requirement would lead to an imaginary number in the denominator of Eq. (2.1), which is physically meaningless. To prevent this from occurring, the Doppler-shifted frequency must be smoothed before it can be further utilized. In the GPS/MET occultation data analysis, we use a constrained matrix smoothing method. It is similar to the linear constrained matrix inversion method (Twomey 1977), which is widely used in other areas of atmospheric remote sensing. Using this method, one can conveniently control the degree of smoothing in different data segments. A brief description of this smoothing method is presented in appendix A. Here we describe its application, along with some typical smoothing results.

Let uppercase bold letters represent matrices and lowercase bold letters represent vectors. The unsmoothed Doppler-shifted frequency series $f_u(t_1)$, $f_u(t_2)$, $f_u(t_3)$, . . . , $f_u(t_K)$ and smoothed Doppler-shifted frequency series $f_s(t_1)$, $f_s(t_2)$, $f_s(t_3)$, . . . , $f_s(t_K)$ may now be seen

as vectors $\mathbf{f}_u$ and $\mathbf{f}_s$ of size K. The matrix smoothing formula using Eq. (A.7) is

$$\mathbf{f}_s = [\mathbf{I} + \mathbf{S}^T\boldsymbol{\Gamma}\mathbf{S}]^{-1}\mathbf{f}_u, \tag{3.1}$$

where $\mathbf{I}$ is the unitary matrix, $\mathbf{S}$ is the constraint smoothing matrix, and $\boldsymbol{\Gamma}$ is a diagonal matrix whose elements control the degrees of smoothing at their corresponding levels. Superscripts T and -1 denote the matrix transpose and inverse.

The unsmoothed Doppler-shifted frequencies $\mathbf{f}_u$ come from the phase measurements and contain the information about the atmosphere to be recovered. However, instrument noise and atmospheric random irregularities along the ray paths inevitably contaminated them. Applying the smoothing matrix $\mathbf{S}$ as in Eq. (3.1) may filter out these contaminants.

There are many different ways to measure smoothness. The smoothing measure used in this paper is to minimize the sum of squares of the third derivatives of the unsmoothed vector $\mathbf{f}_u$ with respect to time t (Twomey 1977). The smaller the sum of squares of the third derivatives, the smoother the function. Using this criterion, the $\mathbf{S}$ matrix can be shown to be

$$\mathbf{S} = \begin{vmatrix} 0 & 0 & 0 & 0 & 0 & 0 & 0 \\ -1 & 2 & -1 & 0 & 0 & 0 & 0 \\ 1 & -3 & 3 & -1 & 0 & 0 & 0 \\ 0 & 1 & -3 & 3 & -1 & 0 & 0 \\ 0 & 0 & 1 & -3 & 3 & -1 & 0 \\ 0 & 0 & 0 & 1 & -3 & 3 & -1 \\ 0 & 0 & 0 & 0 & -1 & 2 & 1 \end{vmatrix}. \tag{3.2}$$

Note that, just for illustration, the $\mathbf{S}$ matrix happens to be (7×7). In real applications, the size of $\mathbf{S}$ depends upon the data size. For instance, if one has a Doppler-shifted frequency series, $f(t_K)$, with $K = 2000$, $\mathbf{S}$ is a matrix of size (2000×2000).

The values of the diagonal matrix $\boldsymbol{\Gamma}$ are selected according to the smoothness desired and the noisiness of the unsmoothed data around each level. They control the strength of the third derivative smoothing. Larger $\boldsymbol{\Gamma}(i, i)$ indicate greater smoothing, and vice versa. Two extreme cases demonstrate the compromise role of $\boldsymbol{\Gamma}(i, i)$. If $\boldsymbol{\Gamma}(i, i) = 0$ for all i, Eq. (3.1) becomes simply $\mathbf{f}_s = \mathbf{f}_u$, which means no smoothing at all. On the other hand, if $\boldsymbol{\Gamma}(i, i)$ approaches infinity, $\mathbf{f}_s$ becomes the smoothest in terms of the above criterion but bears no resemblance at all to $\mathbf{f}_u$. In the simple cases, $\boldsymbol{\Gamma}(i, i)$ may be a constant for all i from 1 to K, or one may change $\boldsymbol{\Gamma}(i, i)$ with i to accommodate varying degrees of smoothing. The numeric values of $\boldsymbol{\Gamma}(i, i)$ do not need to be precise; they are chosen by trial and error.

In the GPS/MET retrievals, we employ a varying $\boldsymbol{\Gamma}(i, i)$ at different altitude (time) levels. At high altitudes, say $\sim$50 km, the relative Doppler-shifted frequency fluctuations $(\Delta f/f)$ are bigger because there the Doppler-shifted frequencies themselves are very small; at lower altitudes, say below 7 km, the relative Doppler fluctuations $(\Delta f/f)$ become bigger again because the atmosphere has more irregularities. To accommodate these situations, $\boldsymbol{\Gamma}(i, i)$ assumes a larger value at 50 km, then decreases with altitude until $\sim$10 km. Below $\sim$10 km, $\boldsymbol{\Gamma}(i, i)$ values increase again with decreasing altitude. With $\boldsymbol{\Gamma}$ varying in this fashion, we can effectively control the oscillation-like behavior commonly shown in the top segment of the retrieved temperature profiles.

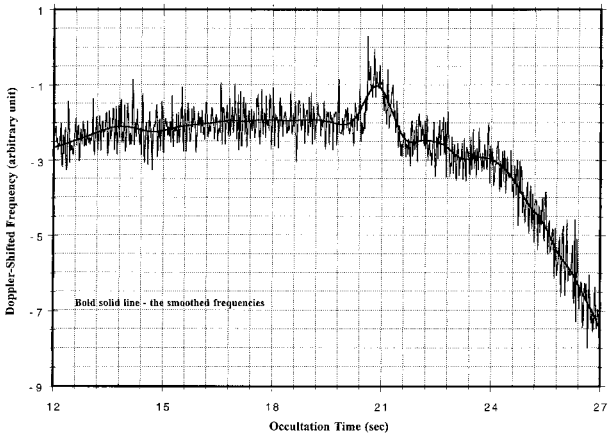

FIG. 4. Smoothed and unsmoothed Doppler-shifted frequencies. The raw (unsmoothed) frequencies are the L1 frequencies from occ0171_03.15_95.294.

The effects of the constrained matrix smoothing technique are shown in Fig. 4. This figure plots both the unsmoothed Doppler-shifted frequency and the smoothed Doppler-shifted frequency. The entire occultation has 2500 records (epochs) in a time stretch of $\sim$50 s. To see the details, only a small section of data is depicted. Nevertheless, high-frequency fluctuations, which are presumably caused by random noise in the raw data, have been largely suppressed.

3) CONVERT THE 3D COORDINATE SYSTEM INTO THE 2D COORDINATE SYSTEM

The GPS and the LEO are all in three-dimensional (3D) motion in the earth-centered coordinate system. During each occultation, the centers of the three bodies define an occultation plane. To simplify computations, however, this three-body, 3D system can be converted into a two-dimensional (2D) coordinate system (Fig. 2) using three Eulerian angles. In this 2D coordinate system, the center of the earth is still the origin O of the coordinates. The LEO is always located on the negative z axis at L with $\mathrm{OL} = -r_{\mathrm{LEO}}$. The positive x axis is defined so that the GPS is somewhere in the first quadrant with $\mathrm{OG} = r_{\mathrm{GPS}}$. Note that only the velocity components of the GPS and LEO that lie in the occultation plane can contribute to the observed Doppler-shifted frequencies. More specifically, only the projection of the GPS velocity vector $\mathbf{v}_{\mathrm{GPS}}$ on line $\mathrm{GC_G}$ and the pro-

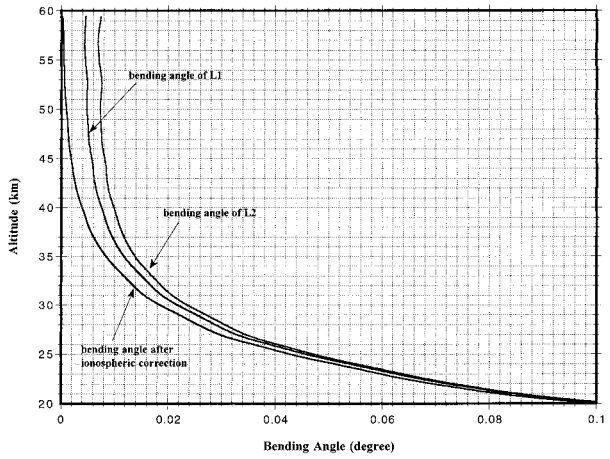

FIG. 5. Ionospheric corrected and uncorrected radio ray bending angles. Bending angle data are from occ0226_03.15_95.291.

jection of the LEO velocity vector $\mathbf{v}_{\mathrm{LEO}}$ on line $\mathrm{LC_L}$ can contribute to the measured Doppler-shifted frequencies.

4) CALCULATE THE BENDING ANGLE AND THE IMPACT DISTANCE

Examination of the relationship among the angles in Fig. 2 leads to the following expression for the Doppler-shifted frequency:

$$f_d = f_0 - \frac{f_0}{c}[v_{lx}\sin(\delta_s + \delta_r) + v_{lz}\cos(\delta_s + \delta_r) - v_{gx}\cos(\beta_e + \beta_r) - v_{gz}\sin(\beta_e + \beta_r)], \quad (3.3)$$

where c is the speed of light in the vacuum; v_{gx}, v_{gz} and v_{lx}, v_{lz} are x- and z-velocity components of the GPS and LEO, respectively, and are known from precision orbit determination; and f_0 represents the nominal GPS transmitter frequencies. In addition, for a spherically stratified atmosphere, the impact distances on both the GPS and LEO sides must be equal. This constraint leads to

$$r_{\mathrm{LEO}}\sin(\delta_s + \delta_r) = r_{\mathrm{GPS}}\sin(\beta_e + \beta_r - \gamma). \quad (3.4)$$

At each occultation epoch, Eqs. (3.3) and (3.4) may be solved iteratively for angles δ_r and β_r (Fig. 2), since r_{LEO}, r_{GPS} and γ, β_e, δ_s are precisely known from the ephemerides of the satellites (Fjeldbo et al. 1971). Once knowing δ_r and β_r, calculation of the impact distance $a = r_{\mathrm{LEO}}\sin(\delta_s + \delta_r)$ and the bending angle $\alpha = \delta_r + \beta_r$ is straightforward. This procedure results in $\alpha(t)$ and $a(t)$. From these, a numerical lookup table, $\alpha(a)$, may be constructed.

Some bending angle $\alpha(a)$ curves are plotted in Fig. 5. There are three curves, one for carrier L1 and one for carrier L2. The third curve is the ionospheric corrected $\alpha(a)$ (see the next section). This figure shows only the altitude range between 20 km and 60 km. Below 20 km, the scale of this figure makes it difficult to distinguish the three curves from each other.

5) IONOSPHERIC CORRECTIONS

All L1 and L2 signals must pass through the earth's ionosphere, either once or twice, before they arrive at the LEO. In contrast to the neutral atmosphere, the ionosphere is a dispersive medium; its refractive index is a function of radio frequency and free electron density. Depending upon the perigee altitude and time of day and year, the ionosphere may have significant effects on the observed phases and bending angles. To obtain the refractivity profiles of the neutral atmosphere, the ionospheric effects must be removed. By making use of the dispersive properties of the ionosphere, through the use of two frequencies, L1 and L2, the contributions of the ionosphere to the calculated bending angles may be mostly removed. (To study ionospheric electron distributions, of course, the ionospheric effects must not be removed. After neutral atmospheric corrections, electron density profiles in the ionosphere can be derived from the L1 and L2 phase measurements.)

According to the method of Vorob'ev and Krasil'nikova (1993), the first-order ''ionosphere-free'' bending angle $\alpha(a)$ can be calculated as follows:

$$\alpha(a) = \frac{f_1^2\alpha_1(a) - f_2^2\alpha_2(a)}{f_1^2 - f_2^2}, \quad (3.5)$$

where f_1 and f_2 are the carrier L1 and carrier L2 frequencies, α_1 and α_2 are the L1 and L2 bending angles, and a is the impact distance. We use Eq. (3.5) to correct the ionospheric effects.

The important point in using the above equation is to have the same impact distance for the L1 ray and the L2 ray. Generally, when radio rays L1 and L2 have the same starting and ending points, they do not travel the same paths because of their different impact distances or bending angles. When doing corrections, we use interpolation to find an L2 ray that has the same impact distance as the L1 ray, then apply Eq. (3.5). According to the estimate of Kursinski et al. (1997), using the above corrections, the residual ionospheric effects would convert to a temperature retrieval error of ~1 K at 40 km, ~0.2 K at 20 km in solar maximum daytime. The residual ionospheric effects to the retrieved temperature may be neglected below 40 km in solar maximum nighttime. During the solar minimum, the residual ionospheric effects would be further reduced. The GPS/MET occultations took place near the solar minimum, resulting in smaller ionospheric errors. Based upon the GPS/MET data, however, Rocken et al. (1997) estimated residual ionospheric noise may result in an error of ~1.5 K in temperature at 40 km. This estimate seems more realistic than the one by Kursinski quoted here.

The corrected ionosphere-free bending angle profile is plotted in Fig. 5, along with the uncorrected L1 and L2 bending angle profiles for comparison. These curves

show the significance of ionospheric corrections, especially above the middle stratosphere.

6) RETRIEVAL OF THE REFRACTIVE INDEX PROFILE $\mu(r)$

The Abel Eq. (2.1) transforms $\alpha(a)$ to $\mu(a)$. In practice, one has to stop the integration at some altitude, where the ray impact distance is a_{top}. Hence Eq. (2.1) becomes

$$\mu(a_0) = \exp\left\{\frac{1}{\pi}\int_{a_0}^{a_{\text{top}}} \frac{\alpha(a)\,da}{(a^2 - a_0^2)^{1/2}}\right\} \times \exp\left\{\frac{1}{\pi}\int_{a_{\text{top}}}^{\infty} \frac{\alpha(a)\,da}{(a^2 - a_0^2)^{1/2}}\right\}. \quad (3.6)$$

By choosing $a_{\text{top}} \approx 90$ km, the second exponential term of the above equation may be set to 1, since the atmosphere above such a high altitude is so tenuous that $\alpha(a)$ is virtually zero. This selection would not deteriorate the retrieval results below ~60 km.

After breaking down the atmosphere into K shells, Eq. (3.6) takes the form

$$\mu(a_0) = \exp\left\{\frac{1}{\pi}\sum_{j=2}^{i}\int_{a_j}^{a_{j-1}} \frac{\alpha(a)\,da}{(a^2 - a_0^2)^{1/2}}\right\}, \quad (3.7)$$

where $i = 2, 3, \ldots, K$, and a_0 means a_{i0}. (The first layer is the top layer, and the Kth layer is the lowest layer.)

If each shell thickness $(a_j - a_{j+1})$ is thin enough (as in the case of GPS/MET occultations), $\alpha(a)$ can be accurately approximated as a linear function of the impact distance. In the jth shell from a_{j-1} to a_j, we write

$$\alpha(a) = \alpha(a_{j-1}) + q_j(a - a_{j-1}),$$

where $q_j = [\alpha(a_{j-1}) - \alpha(a_j)]/(a_{j-1} - a_j)$. Then the integral in Eq. (3.7) becomes

$$\int_{a_j}^{a_{j-1}} \frac{\alpha(a)\,da}{(a^2 - a_0^2)^{1/2}} \cong \int_{a_j}^{a_{j-1}} \frac{\alpha(a_{j-1}) - q_j a_{j-1} + q_j a}{(a^2 - a_0^2)^{1/2}}\,da. \quad (3.8)$$

Equation (3.8) can be integrated analytically. In this way, refractive index profile $\mu(a_0)$ or $\mu(r_0)$ can be evaluated accurately. [Recall that $\mu(a_0) = \mu(r_0)$ and $a_0 = \mu(r_0)r_0$; r_0 is the radial distance from the earth to the radio path at perigee point B.]

In real data inversions, we start using the GPS/MET measurements from ~60 km, where the measured bending angles become ≳few $\times 10^{-4}$ degree. Between ~60 km and z_{top}, a calculated bending angle profile from a Cooperative Institute for Research in the Atmosphere (CIRA) atmosphere model (Fleming et al. 1990) corresponding to the occultation latitude, and month of the year is invoked. In the vicinity of the joint altitude, the slopes and values of the model and the data bending angle profiles are gradually adjusted to reconcile the data bending angle profile below the joint region. In this way, a smooth transition from the data profile to the model profile is realized.

A typical retrieved N profile is shown in Fig. 6.

7) RETRIEVALS OF TEMPERATURE AND PRESSURE PROFILES

By using the retrieved N profile along with the equation of state $P = \rho RT$ and hydrostatic equation $dp/dz = -g\rho$, temperature and pressure profiles can be deduced as described in section 2. After replacing the upper infinity limit by $z_{\text{top}} = 90$ km, Eqs. (2.6) and (2.7) may be rewritten as follows:

$$P(z_i) = \frac{1}{R77.6}\int_{z_i}^{90\,\text{km}} g(z')N(z')\,dz' + P(90\,\text{km}) \quad (3.9)$$

$$T(z_i) = \frac{1}{R}\frac{\int_{z_i}^{90\,\text{km}} g(z')N(z')\,dz'}{N(z_i)} + \frac{77.6}{N(z_i)}P(90\text{ km}), \quad (3.10)$$

where $i = 1, 2, \ldots, K$. The integration goes from z_i up to $z = 90$ km. That is high enough because $P(90\text{ km}) = (77.6R)^{-1}\int_{90\,\text{km}}^{\infty} g(z')N(z')\,dz' \approx 2 \times 10^{-3}$ mb. We can ignore such a small additive pressure, provided that we confine the retrieved pressure profile to altitudes below 50 km (pressure P at 50 km $\approx 8 \times 10^{-2}$ mb).

To obtain $T(z_i)$, one encounters the boundary condition on pressure again. The numerical error of the assigned $P(90\text{ km})$ is of no significance in calculating $T(z)$ from Eq. (3.10) for altitudes less than 50 km, because as z_i decreases, the contribution of the second term on the right-hand side of Eq. (3.10) to $T(z_i)$ diminishes rapidly. For example, at $z_i = 50$, 30, and 10 km, $[77.6P(90\text{ km})/N(z_i)]$ is of the order of 0.7, 0.04, and 0.002 K, respectively.

Examples of retrieved temperature and pressure profiles are shown in Figs. 7a,b.

b. Error analysis

All remote sensing measurements and inversion results are subject to errors. Knowledge of these errors is essential for understanding and interpreting the results. In the present case, the uncertainties of N, T, and P profiles inherently depend upon random errors in the measured data. They also depend upon the underlying theoretical formulas (models) as well as the numerical computational schemes used. The latter two factors affect the way the measurement errors propagate in the data analysis process. Generally systematic and random errors may both be present in the measurements and

data analyses. In the GPS/MET occultations, among the systematic errors are the model errors, the atomic frequency drifts, and the uncertainties in satellite ephemerides and velocities. Those uncertainties are highly correlated during each occultation period (typically 60 s) and usually cause biases in the retrievals. In this section, the main concern is how the random noise in the measurements propagates through the inversion process. We examine the statistical uncertainties at the end of the data analysis process to determine whether or not they are the major uncertainties in the GPS/MET retrieved profiles. For other error sources and their impacts upon the overall GPS/MET retrievals, readers are advised to refer to Kursinski et al. (1997).

1) PRINCIPLES OF ERROR PROPAGATION

The noise in the recorded GPS phases comes primarily from random atmospheric irregularities along the ray propagation path and the thermal fluctuations of the GPS receiver. This kind of noise is nearly white Gaussian and stationary over short intervals of time (Lipa and Tyler 1979). In addition, we assume the noises in the measurements are independent and uncorrelated.

The random error analysis used in this paper is based on the principles of the propagation of errors (Brandt 1963). As in matrix smoothing, one may consider a series of measured random data as a data vector $\mathbf{x}$. An operator, $\mathbf{O}$, represents a transform or operation. Operating $\mathbf{O}$ on $\mathbf{x}$ yields vector $\mathbf{y}$, which is also a random series. If the transform is linear, $\mathbf{O}$ maps $\mathbf{x}$ into a new vector $\mathbf{y}$ through $\mathbf{Ox} = \mathbf{y}$. If it is not linear, one can expand $\mathbf{O}$ into a Taylor series around the neighbor of $\overline{\mathbf{x}}$,

$$\mathbf{y}(\mathbf{x}) = \mathbf{y}(\overline{\mathbf{x}}) + \mathbf{O}_1(\mathbf{x} - \overline{\mathbf{x}}) + \text{higher order terms.}$$

Furthermore, if $(\mathbf{x} - \overline{\mathbf{x}})$ is small enough compared with $\overline{\mathbf{x}}$, all terms higher than the first order can be neglected, leaving the linear term only,

$$\mathbf{y}(\mathbf{x}) - \mathbf{y}(\overline{\mathbf{x}}) = \mathbf{O}_1(\mathbf{x} - \overline{\mathbf{x}}). \tag{3.11}$$

Let the dimensions of $\mathbf{x}$ and $\mathbf{y}$ be m and n, respectively. Then the linear operator $\mathbf{O}_1$, evaluated at $\overline{\mathbf{x}}$, takes the following structure (Brandt 1963):

$$\mathbf{O}_1 = \begin{vmatrix} \frac{\partial y_1}{\partial x_1} & \frac{\partial y_1}{\partial x_2} & \cdots & \frac{\partial y_1}{\partial x_m} \\ \frac{\partial y_2}{\partial x_1} & \frac{\partial y_2}{\partial x_2} & \cdots & \frac{\partial y_2}{\partial x_m} \\ \cdot & \cdot & \cdots & \cdot \\ \cdot & \cdot & \cdots & \cdot \\ \frac{\partial y_n}{\partial x_1} & \frac{\partial y_n}{\partial x_2} & \cdots & \frac{\partial y_n}{\partial x_m} \end{vmatrix}. \tag{3.12}$$

In the GPS/MET occultations, $(\mathbf{x} - \overline{\mathbf{x}})$ in Eq. (3.11) may be thought of as the random measurement errors of the variable $\mathbf{x}$ around its true value, $\overline{\mathbf{x}}$. Therefore, by definition, the covariance matrices $\mathbf{C}_x$ for $\mathbf{x}$ and $\mathbf{C}_y$ for $\mathbf{y}$ are $\langle(\mathbf{x} - \overline{\mathbf{x}})(\mathbf{x} - \overline{\mathbf{x}})^{\mathrm{T}}\rangle$ and $\langle(\mathbf{y} - \overline{\mathbf{y}})(\mathbf{y} - \overline{\mathbf{y}})^{\mathrm{T}}\rangle$, respectively, where the angle bracket means statistical expectation and the superscript T represents the transpose matrix. Furthermore, because of Eq. (3.11), $\mathbf{C}_y$ may be related to $\mathbf{C}_x$ as follows ($\mathbf{O}_1$ has been replaced by $\mathbf{O}$):

$$\mathbf{C}_y = \langle(\mathbf{y} - \overline{\mathbf{y}})(\mathbf{y} - \overline{\mathbf{y}})^{\mathrm{T}}\rangle = \mathbf{O}\mathbf{C}_x\mathbf{O}^{\mathrm{T}}. \tag{3.13}$$

Data analysis usually requires many consecutive operations. The general operator $\mathbf{O}$ is the product of each component operator, $\mathbf{O}_x$; that is, $\mathbf{O} = (\mathbf{O}_a\mathbf{O}_b\mathbf{O}_c \cdots)$. Each $\mathbf{O}_x$ carries out a specific task, such as that described in each square box in Fig. 3. Consequently, the covariance matrix for y becomes

$$\mathbf{C}_y = (\mathbf{O}_a\mathbf{O}_b\mathbf{O}_c \cdots)\mathbf{C}_x(\mathbf{O}_a\mathbf{O}_b\mathbf{O}_c \cdots)^{\mathrm{T}}. \tag{3.14}$$

This is the equation we applied for estimating the covariances of the retrieved profiles. The square roots of the diagonal elements of $\mathbf{C}_y$ are the standard deviations of the retrieved N, P, and T's.

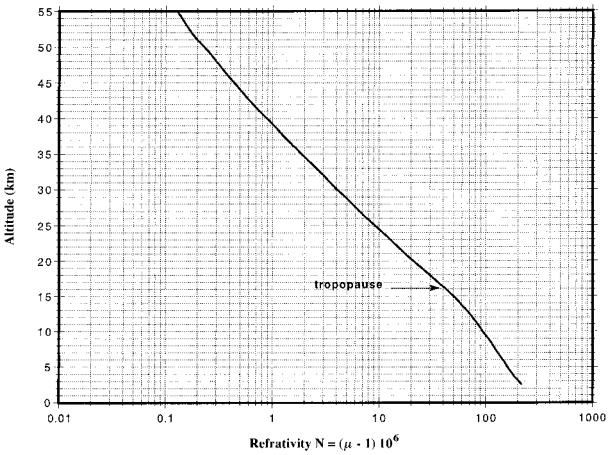

FIG. 6. Refractivity profile from the GPS/MET occultation occ0226_03.15_95.291. Note evident slope change around 16 km, the tropopause height. (See Fig. 7.)

2) FORMULAS FOR ESTIMATING STATISTICAL RETRIEVAL UNCERTAINTIES

We start with the covariance matrix $\mathbf{C}_f$ for the Doppler-shifted frequency $\mathbf{f}_d$:

$$\mathbf{C}_f = \langle(\mathbf{f}_d - \overline{\mathbf{f}}_d)(\mathbf{f}_d - \overline{\mathbf{f}}_d)^{\mathrm{T}}\rangle = \langle\Delta\mathbf{f}_d\Delta\mathbf{f}_d^{\mathrm{T}}\rangle. \tag{3.15}$$

In calculating $\mathbf{C}_f$, $\mathbf{f}_d$ represents the measured data, but what are the $\Delta\mathbf{f}_d(i)$'s? To find each $\Delta\mathbf{f}_d(i)$, we adapted a method suggested by Jenkins and Steffes (1991). First, fit the series $\mathbf{f}_d(t_{i-k})$, $\mathbf{f}_d(t_{i-(k-1)})$, . . . , $\mathbf{f}_d(t_{i-1})$, $\mathbf{f}_d(t_i)$, $\mathbf{f}_d(t_{i+1})$, . . . , $\mathbf{f}_d(t_{i+k})$ (we use $k = 9$) for every t_i with a quadratic curve. Second, take the square root of the mean of the squared differences between $\mathbf{f}_d$ and the quadratic fitting as the desired $\Delta\mathbf{f}_d(i)$. After the $\Delta\mathbf{f}_d(i)$'s are known, $\mathbf{C}_f$ can be evaluated.

The covariance matrix $\mathbf{C}_N$ for refractivity N and the

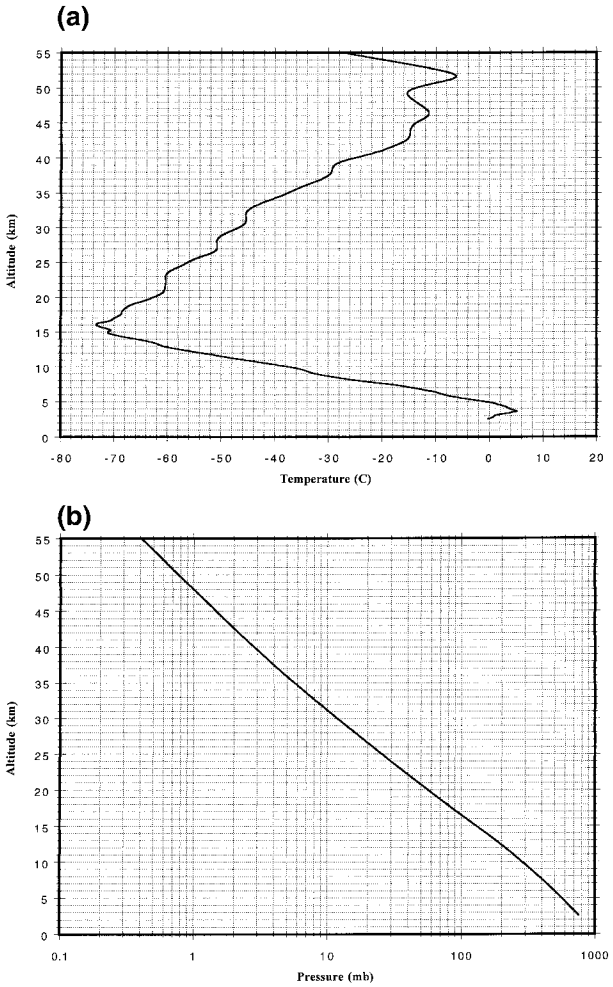

FIG. 7. (a) Temperature profile from GPS/MET occultation occ0226_03.15_95.291. The abrupt turning to the left of the retrieved temperature around 4 km is primarily caused by water vapor because the (dry) temperature is retrieved with the assumption of a dry atmosphere. (b) Pressure profile from GPS/MET occultation occ0226_03.15_95.291.

covariance matrix $\mathbf{C}_T$ for temperature T are derived from $\mathbf{C}_f$ using the following expressions:

$$\mathbf{C}_N = \langle(\mathbf{T}_{N\text{imp}}\mathbf{T}_{\text{imp}} + \mathbf{T}_{N\text{alp}}\mathbf{T}_{\text{alp}}) \times \mathbf{C}_f(\mathbf{T}_{N\text{imp}}\mathbf{T}_{\text{imp}} + \mathbf{T}_{N\text{alp}}\mathbf{T}_{\text{alp}})^{\text{T}}\rangle \quad (3.16)$$

$$\mathbf{C}_T = \langle[\mathbf{T}_{\text{tem}}(\mathbf{T}_{N\text{imp}}\mathbf{T}_{\text{imp}} + \mathbf{T}_{N\text{alp}}\mathbf{T}_{\text{alp}})] \times \mathbf{C}_f[\mathbf{T}_{\text{tem}}(\mathbf{T}_{N\text{imp}}\mathbf{T}_{\text{imp}} + \mathbf{T}_{N\text{alp}}\mathbf{T}_{\text{alp}})]^{\text{T}}\rangle. \quad (3.17)$$

The matrices in the above expressions, $\mathbf{T}_{N\text{imp}}$, $\mathbf{T}_{\text{imp}}$, $\mathbf{T}_{N\text{alp}}$, $\mathbf{T}_{\text{alp}}$, and $\mathbf{T}_{\text{tem}}$, may be found in appendix B. The statistical uncertainties for the retrieved refractivity δN and for the retrieved temperature δT at the ith layer are then given as

$$\delta N(i) = \sqrt{C_N(i, i)}; \qquad \delta T(i) = \sqrt{C_T(i, i)}. \quad (3.18)$$

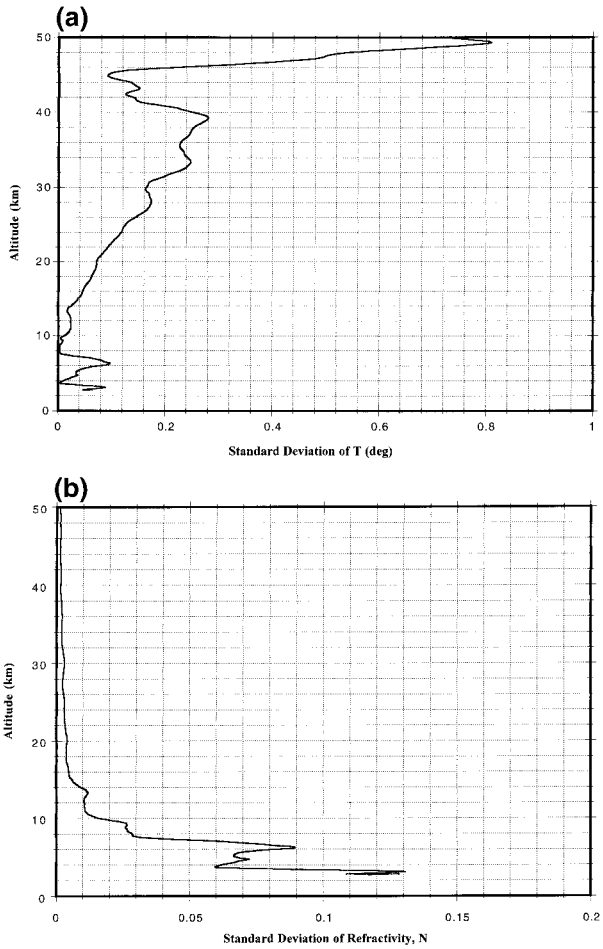

FIG. 8. (a) Standard deviation of retrieved temperature for GPS/MET occultation occ0226_03.15_95.291. (b) Standard deviation of refractivity, N, for GPS/MET occultation occ0226_03.15_95.291.

For occultation #226 of 1 July 1995, these uncertainties are estimated and plotted in Fig. 8. Figures 8a and 8b are the retrieved temperature and refractivity uncertainties.

The estimated uncertainties in this section are statistical uncertainties only. In the upper stratosphere, imperfect ionospheric corrections lead to larger uncertainties than the statistical ones presented here. In the lower part of the troposphere, unpredictable water vapor distribution and multipath problems affect the retrieval accuracies (Kursinski et al. 1997). According to Rocken et al. (1997), the overall retrieved refractivity error is about 0.5%, corresponding to a retrieved temperature error of $\sim\pm1$°C from 1 to ~40 km. Therefore, the statistical errors are not significant in the overall GPS/MET retrieval error budget.

4. GPS/MET data analysis results and summary

To illustrate the data analysis results of the GPS/MET atmospheric sounding, four temperature profiles (tem-

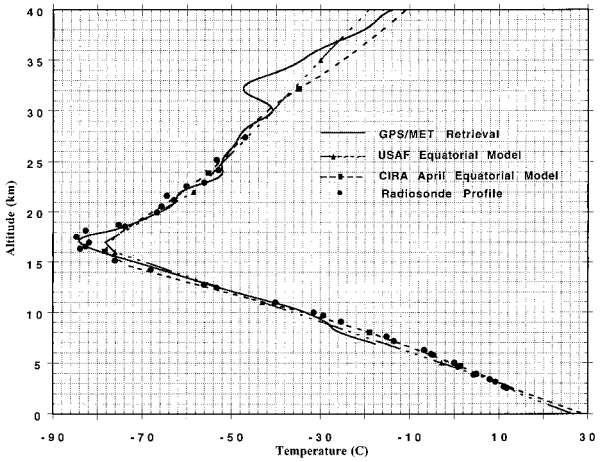

FIG. 9. The first retrieved GPS/MET temperature profile and its comparison with radiosonde measurements and other temperature models.

perature vs altitude and pressure vs altitude) are presented here. Readers who wish to have more retrieved profiles and detailed descriptions may refer to Ware et al. (1996) and Rocken et al. (1997).

Figure 9 is the first known GPS/MET temperature inversion produced by The University of Arizona. This occultation took place over the equatorial region north of the mountainous Colombia–Ecuador border (2°N, 78°W) on 16 April 1995, 13 days after the launch of *MicroLab-1*. For comparison, the U.S. Air Force and CIRA equatorial model temperature profiles, as well as the nearby radiosonde profile, are coplotted. This first profile was retrieved using several simplifications, including 1 Hz occultation data. Nevertheless, the agreement with the radiosonde data between 9 and 30 km turns out to be remarkably good. Particularly, the GPS/MET profile accurately resolves the height and temperature of the tropopause. The kink around 32 km in this profile seems suspicious. We could not confirm it because no other observations existed around that height. It might be real to some degree. Below 9 km, the GPS/MET profile begins exhibiting a bias toward the cold side (the so-called dry temperature). This cold bias is almost certainly due to the neglect of water vapor there in the lower troposphere.

The occultation in Fig. 10 occurred over the Volcano Islands in the Pacific, approximately 1000 km south of Tokyo, Japan. Figure 10a shows altitude versus temperature; Figure 10b shows pressure versus temperature. The National Meteorological Center (NMC) data are derived from its global analysis and interpolated to the occultation time and location. The other data profiles in these two figures were collected a few hundred kilometers away and several hours apart from the GPS/MET occultation location and time. In the figures, both radiosonde and NMC data stop at ~31 km, but from 31 to 11 km (10 to ~300 mb) they are in good agreement with the GPS/MET profiles. Again, the GPS/MET profile accurately reveals the tropopause. In the upper stratosphere between 50 (~1 mb) and 40 km (~4 mb), the difference between GPS/MET and STRAT (the Stratospheric Tracers of Atmospheric Transport experiment) is less than 10°C. (We do not know the accuracy of STRAT.) Because of the occultation location and season, a considerable amount of water vapor existed in the lower part of the troposphere there. The irregular

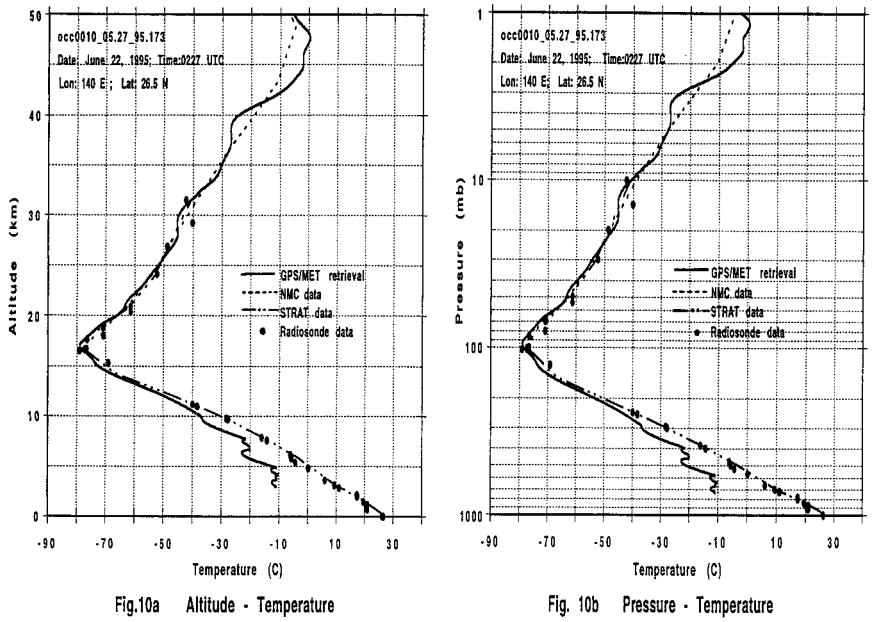

FIG. 10. GPS/MET retrievals: (a) altitude vs temperature and (b) pressure vs temperature. See the text for details.

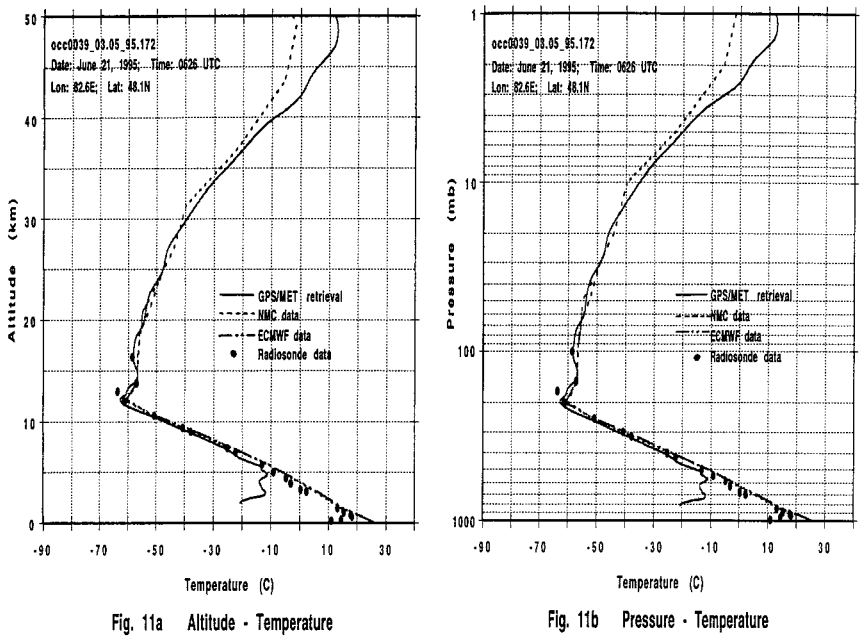

FIG. 11. GPS/MET retrievals: (a) altitude vs temperature and (b) pressure vs temperature. See the text for details.

water vapor distribution produced the fluctuation and cold deviation of GPS/MET temperature from the radiosonde temperature below 9 km.

Figure 11 describes an occultation that occurred over Zajsan, Kazakhstan, on 21 June 1995. The radiosonde location is about 400 km away from the occultation location. Similar to other cases, the GPS/MET and radiosonde data agree with each other very well from 6 to 40 km. Below 4.5 km, neglect of water vapor heavily affects the behavior of the GPS/MET profiles. Above 40 km, the GPS/MET and the NMC profiles also display greater differences. Without knowing the accuracy of NMC data at that height, it is hard to judge which profile is closer to the true temperature distribution.

Figure 12 represents an occultation carried out over Kimberley, Canada (600 km east of Vancouver). The other observation and analysis data were available only below 32 km ($\sim$10 mb). Like the other occultation cases, the water vapor impact on the retrieved dry temperature becomes profound below $\sim$7 km.

One may notice that in Fig. 12 the GPS/MET profiles show some wave-like oscillations above 40 km. Actually this kind of oscillation feature is not an exception, but rather a common feature in the GPS/MET temperature retrievals. Generally when the degree of smoothing is lessened, these oscillations appear in the temperature profiles. Among other causes, free electron density fluctuations in the ionosphere could generate similar oscillation structures in the retrieved temperature profiles. On the other hand, possible atmospheric waves could also cause these wavelike structures. These different possibilities reduce our confidence in the temperature retrievals above 40 km. Further studies are needed to clarify this situation.

The other major retrieval problem concerns the lower part of the troposphere. In this region, atmospheric defocusing, turbulence, and inhomogeneity, especially when associated with unpredictable water vapor distribution, cause weak signal-to-noise ratio and multipath.

The multipath problem is primarily induced by considerable and irregular water vapor distributions in the lower troposphere. In the hydrostatic earth atmosphere, there is usually only one single path linking the transmitter and the receiver. Because radio rays bend toward the region of higher refractive index (Born and Wolf 1959), if irregularly distributed and significant amounts of water vapor are present in the atmosphere, there may possibly be more than one path connecting the GPS and the LEO, causing phase interference at the input port of the receiver. The resultant phase received by the receiver aboard the LEO is unpredictable and bears no resemblance to the phase received in the single-path case in the severe multipath environment. Therefore, multipath, if it occurs, produces false phase relationships with time, causing larger errors in refractivity and temperature retrievals. In the worst case, multipath could force the phase-locked receiver to stop phase measurements. Recently, using the principles of wave optics, Gorbunov and Gurvich (1998) applied the diffraction correction method to the multipath problem. Their results are very encouraging. In the future, occultation experiments using improved instrumentation and antennas with better directivity may also contribute to the solution of the multipath problem.

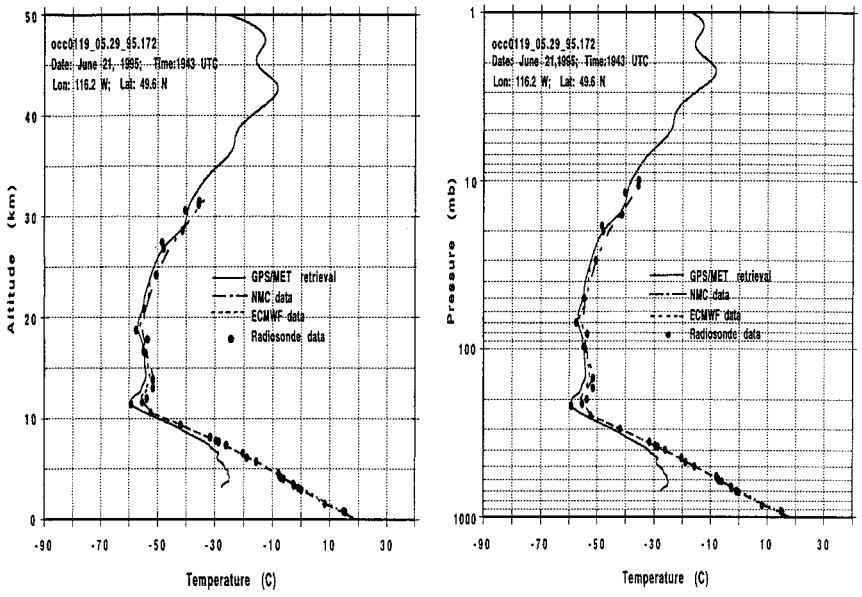

FIG. 12. GPS/MET retrievals: (a) altitude vs temperature and (b) pressure vs temperature. See the text for details.

In spite of the problems discussed above, the GPS/MET occultation has proved itself to be a successful and feasible technique for remotely sensing the earth's atmosphere. Without the multipath corrections, the GPS/MET temperature profiles are able to be reliable and accurate to within 1°–2°C from ~5–7 to ~40 km above the ground. The retrievals shown in Figs. 9–12 are without the multipath corrections. After applying the multipath corrections, comparisons with radiosonde and other observations and with numerical analysis data have suggested that the temperature profiles are statistically accurate to within ±1°C from 1 to ~40 km above the ground (Rocken et al. 1997). The vertical resolution of the GPS/MET radio occultation sounding is constrained by the diffraction limit (the first Fresnel zone), and it ranges from a few hundred meters near the ground to ~1.5 km in the upper stratosphere (Kursinski et al. 1993). The horizontal resolution, about 200 km, is related to the ray path length in the lowest atmospheric layer that the radio ray is able to penetrate (Melbourne et al. 1994). Although this horizontal resolution seems relatively poor compared with the vertical one, it is in fact somewhat of an advantage in the mesoscale weather analysis and the research of global change. Eyre (1994) first suggested that directly using the refraction (bending) angles from the GPS/MET measurements, rather than using P and T profiles, is advantageous in numerical weather prediction. This concept circumvents the inseparable water vapor factor from the GPS/MET temperature profiles and enhances the applications of the GPS/MET sounding to numerical weather prediction [Zou et al. 1995, 1998, manuscript submitted to *J. Geophys. Res.* (*Atmos.*); Kuo et al. 1998], since the bending angles intrinsically contain the water vapor effects. Nevertheless, for the time being, the single LEO GPS/MET atmospheric sounding is too sparse in space, and in time as well, to be of much value for mesoscale research and operations. Until a LEO constellation has been established, the GPS/MET occultation sounding will likely retain its experimental status.

Acknowledgments. The authors thank M. Exner, M. E. Gorbunov, W. Schreiner, and S. V. Sokolovskiy for the numerous discussions during the development of the GPS/MET data analysis algorithm. They also thank M. Sanderson-Rae for editing the final manuscript. This work was supported by the University Corporation for Atmospheric Research (UCAR) under Contract 412880.

APPENDIX A

Constrained Matrix Smoothing Method

In atmospheric remote sensing, the following integral equation is frequently encountered:

$$\int_a^b A(x, y) f(x)\, dx = g(y), \qquad \text{(A.1)}$$

where $A(x, y)$, a function of variables x and y, is the kernel; $f(x)$ and $g(y)$ are the unknown function and the measurements (data), respectively. The data $g(y)$ are subject to random noise and the measurement error. The kernel $A(x, y)$ depends upon the physics and models of the problem under investigation. The task of remote

sensing is to find $f(x)$, which satisfies Eq. (A.1), from the measurement $g(y)$.

In numerical computations, one generally has to replace the above integral by a summation,

$$\sum_{j=1}^{M} A(y_i, x_j) f(x_j) = g(y_i), \qquad i = 1, 2, \ldots, N,$$

where N is the number of measurements and M is the number of the unknown $f(x)$'s. Then using vector–matrix notation, the above can be rewritten as

$$\mathbf{Af} = \mathbf{g}, \tag{A.2}$$

where $\mathbf{A}$ is an $(N \times M)$ matrix, and $\mathbf{f}$ and $\mathbf{g}$ are vectors of $(M \times 1)$ and $(N \times 1)$, respectively. In practice, N is likely greater than or equal to M. Therefore, solving Eq. (A.2) for $\mathbf{f}$ in the least squares sense gives

$$\mathbf{f} = (\mathbf{A}^T\mathbf{A})^{-1}\mathbf{A}^T\mathbf{g}. \tag{A.3}$$

In the above equation, superscripts T and -1 represent the transpose and inverse matrix.

For many remote sensing problems, however, this inversion formula (A.3) fails to work out a stable solution because of the numerically ill-conditioned kernel matrix $\mathbf{A}$ and/or the noise in the measurements $\mathbf{g}$. To deal with the instability in the above inverted $\mathbf{f}$, Twomey (1977) developed a linear constrained matrix inversion method,

$$\mathbf{f} = (\mathbf{A}^T\mathbf{A} + \gamma\mathbf{H})^{-1}\mathbf{A}^T\mathbf{g}. \tag{A.4}$$

In this equation, γ is the undetermined Lagrangian multiplier, which is chosen by trial and error, and $\mathbf{H}$ is a square matrix. Actually, $\mathbf{H} = \mathbf{S}^T\mathbf{S}$, where $\mathbf{S}$ is a smoothing matrix of $(M \times M)$; $\mathbf{S}$ may have a different structure. For example, if a smoothing criterion is to minimize the sums of the squares of solution $\mathbf{f}$'s second differences, $\mathbf{S}$ becomes (Twomey 1977)

$$\mathbf{S} = \begin{vmatrix} 0 & 0 & 0 & 0 & 0 & 0 \\ -1 & 2 & -1 & 0 & 0 & 0 \\ 0 & -1 & 2 & -1 & 0 & 0 \\ 0 & 0 & -1 & 2 & -1 & 0 \\ 0 & 0 & 0 & -1 & 2 & -1 \\ . & . & . & . & . & . \end{vmatrix}. \tag{A.5}$$

If a smoothing criterion is to minimize the sums of the squares of solution $\mathbf{f}$'s third differences, $\mathbf{S}$ then becomes Eq. (3.2). Note that in Twomey's Eq. (A.4), γ is a single constant.

Generally one can assign a varying $\gamma = \gamma(i)$ to accommodate varying degrees of smoothing. In such a case, the following formula should be applied:

$$\mathbf{f} = (\mathbf{A}^T\mathbf{A} + \mathbf{S}^T\mathbf{\Gamma S})^{-1}\mathbf{A}^T\mathbf{g}, \tag{A.6}$$

where $\mathbf{\Gamma}$ is a diagonal matrix of size $(M \times M)$ with $\mathbf{\Gamma}(i, i) = \gamma(i)$.

The above linear constrained matrix inversion formula may also be used for smoothing noise-contaminated data. In doing so, let data $\mathbf{g}$ be $\mathbf{f}_u$, and replace matrix $\mathbf{A}$ with the unitary matrix $\mathbf{I}$. Thus, Eq. (A.2) formally becomes

$$\mathbf{If}_s = \mathbf{f}_u,$$

where $\mathbf{f}_u$ is the unsmoothed data and $\mathbf{f}_s$ is the smoothed data. Accordingly, Eq. (A.6) should be rewritten as

$$\mathbf{f}_s = (\mathbf{I}^T\mathbf{I} + \mathbf{S}^T\mathbf{\Gamma S})^{-1}\mathbf{I}^T\mathbf{f}_u = (\mathbf{I} + \mathbf{S}^T\mathbf{\Gamma S})^{-1}\mathbf{f}_u. \tag{A.7}$$

Equation (A.7) here is Eq. (3.1) in the text.

APPENDIX B

Formulas Used in the Error Analysis

In this appendix, we list the expressions for $\mathbf{T}_{N\text{imp}}$, $\mathbf{T}_{\text{imp}}$, $\mathbf{T}_{N\text{alp}}$, $\mathbf{T}_{\text{alp}}$, and $\mathbf{T}_{\text{tom}}$ used in the statistical error estimates. All letters represent the same variables as used in the text.

$$\mathbf{T}_{N\text{imp}}(i,1) = (\alpha_1 + \alpha_2)\frac{1}{(a_1^2 - a_i^2)^{1/2}}, \qquad i \geq 2$$

$$\mathbf{T}_{N\text{imp}}(i,j) = (\alpha_{j+1} - \alpha_{j-1})\frac{1}{(a_j^2 - a_i^2)^{1/2}}, \qquad i \geq 2, 2 \leq j < i$$

$$\mathbf{T}_{N\text{imp}}(i,i) = -(\alpha_{i-1} + \alpha_i)\frac{1}{a_i}, \qquad i \geq 2$$

$$\mathbf{T}_{N\text{alp}}(i,1) = \ln\frac{a_1 + (a_1^2 - a_i^2)^{1/2}}{a_2 + (a_2^2 - a_i^2)^{1/2}}, \qquad i \geq 2$$

$$\mathbf{T}_{N\text{alp}}(i,j) = \ln\frac{a_{j-1} + (a_{j-1}^2 - a_i^2)^{1/2}}{a_{j+1} + (a_{j+1}^2 - a_i^2)^{1/2}}, \qquad i \geq 2, 2 \leq j < i$$

$$\mathbf{T}_{N\text{alp}}(i,i) = \ln\frac{a_{i-1} + (a_{i-1}^2 - a_i^2)^{1/2}}{a_i}, \qquad i \geq 2$$

$$\mathbf{T}_{N\text{imp}}(1,1) = \mathbf{T}_{N\text{alp}}(1,1) = 0.$$

Because $\mathbf{T}_{N\text{imp}}(i, j)$ and $\mathbf{T}_{N\text{alp}}(i, j)$ are all zero for $j > i$, they both are lower triangle matrices.

The matrices $\mathbf{T}_{\text{alp}}$ and $\mathbf{T}_{\text{imp}}$ are diagonal with $\mathbf{T}_{\text{alp}}(i, j) = \mathbf{T}_{\text{imp}}(i, j) = 0$, for $i \neq j$, and

$$\mathbf{T}_{\text{alp}}(i, i) = \left[1 + \frac{\frac{r_{\text{GPS}}}{r_{\text{LEO}}}\cos(\beta_e - \gamma + \beta_r)}{\left[1 - \left(\frac{r_{\text{GPS}}}{r_{\text{LEO}}}\right)^2 \sin^2(\beta_e - \gamma + \beta_r)\right]^{1/2}}\right]\frac{\partial\beta_r}{\partial f_d}$$

$$\mathbf{T}_{\text{imp}}(i, i) = r_{\text{GPS}}\cos(\beta_e - \gamma + \beta_r)\left(\frac{\partial\beta_r}{\partial f_d}\right),$$

where $\partial\beta_r/\partial f_d$ can be determined with Eq. (3.3) in the text:

$$\mathbf{T}_{\text{tem}}(i, i) = \frac{b_i - T_i}{N_i} \qquad j = i$$

$$\mathbf{T}_{\text{tem}}(i, j) = \frac{b_j}{N_i}, \qquad j < i$$

where

$$b_j = T_j \qquad j = 1$$

$$b_j = \frac{g}{R}(z_{j-1} - z_j) \qquad j \geq 2.$$

REFERENCES

Born, M., and E. Wolf, 1959: *Principles of Optics.* Pergamon, 803 pp.

Brandt, S., 1963: *Statistical and Computational Methods in Data Analysis.* North-Holland, 323 pp.

Eshleman, V. R., 1973: The radio occultation method for the study of planetary atmospheres. *Planet. Space Sci.,* **21,** 1521–1531.

Eyre, J. R., 1994: Assimilation of radio occultation measurements into a numerical weather prediction system. European Centre for Medium-Range Weather Forecasts Tech. Memo. 199, 34 pp.

Fjeldbo, G. F., and V. R. Eshleman, 1968: The atmosphere of Mars analyzed by integral inversion of the Mariner IV occultation data. *Planet. Space Sci.,* **16,** 1035–1059.

——, A. J. Kliore, and V. R. Eshleman, 1971: The neutral atmosphere of Venus as studied with the Mariner V radio occultation experiments. *Astron. J.,* **76,** 123–140.

Fleming, E. L., S. Chandra, J. J. Barnett, and M. Corney, 1990: Zonal mean temperature, pressure, zonal wind and geopotential height as functions of latitude. *Adv. Space Res.,* **10,** 11–59.

Gorbunov, M. E., and A. S. Gurvich, 1998: Microlab-1 experiment: Multipath effects in the lower troposphere. *J. Geophys. Res.,* **103,** 13 818–13 826.

Hinson, D. P., and J. M. Jenkins, 1995: Magellan radio occultation measurements of atmospheric waves on Venus. *Icarus,* **114,** 310–327.

Hofmann-Wellenhof, B., H. Lichtenegger, and J. Collins, 1997: *Global Positioning System: Theory and Practice.* Springer-Verlag, 389 pp.

Jenkins, J. M., and P. G. Steffes, 1991: Results for 13-cm absorptivity and H_2SO_4 abundance profiles from the season 10 (1986) Pioneer Venus orbiter radio occultation experiment. *Icarus,* **90,** 129–138.

——, and ——, 1994: Radio occultation studies of the Venus atmosphere with the Magellan spacecraft: 2. Results from the October 1991 experiments. *Icarus,* **110,** 79–94.

Kliore, A. J., D. L. Cain, G. S. Levy, V. R. Eshleman, G. Fjeldbo, and F. D. Drake, 1965: Occultation experiment: Results of the first direct measurement of Mars' atmosphere and ionosphere. *Science,* **149,** 1243–1248.

Kuo, Y.-H., X. Zou, and W. Huang, 1998: The impact of Global Positioning System data on the prediction of an extratropical cyclone: An observing system simulation experiment. *Dyn. Atmos. Oceans,* **27,** 439–470.

Kursinski, E. R., G. A. Hajj, and K. R. Hardy, 1993: Temperature or moisture profiles from radio occultation measurements. Preprints, *Eighth Symp. on Meteorological Observations and Instrumentation,* Anaheim, CA, Amer. Meteor. Soc., J153–J158.

——, ——, ——, L. J. Romans, and J. T. Schofield, 1995: Observing tropospheric water vapor by radio occultation using the Global Positioning System. *Geophys. Res. Lett.,* **22,** 2365–2368.

——, and Coauthors, 1996: Initial results of radio occultation observations of earth's atmosphere using the Global Positioning System. *Science,* **271,** 1107–1110.

——, ——, J. T. Schofield, R. P. Linfield, and K. R. Hardy, 1997: Observing earth's atmosphere with radio occultation measurements using the Global Positioning System. *J. Geophys. Res.,* **102,** 23 429–23 465.

Liebe, H. J., 1989: MPM—An atmospheric millmeter-wave propagation model. *Int. J. Infrared Millimeter Waves,* **10,** 631–650.

Lindal, G. F., 1992: The atmosphere of Neptune: An analysis of radio occultation data acquired with Voyager 2. *Astron. J.,* **103,** 967–982.

——, H. B. Hotz, D. N. Sweetnam, Z. Shippony, J. P. Bernkle, G. V. Hartsell, R. T. Spear, and W. H. Michael, 1979: Viking radio occultation measurements of the atmosphere and topography of Mars: Data acquired during 1 Martian year of tracking. *J. Geophys. Res.,* **84,** 8443–8456.

——, and Coauthors, 1981: The atmosphere of Jupiter: An analysis of the Voyager radio occultation measurements. *J. Geophys. Res.,* **86,** 8721–8727.

——, ——, H. B. Hotz, D. N. Sweetnam, V. R. Eshleman, and G. L. Tyler, 1983: The atmosphere of Titan: An analysis of the Voyager 1 radio occultation measurements. *Icarus,* **53,** 348–363.

——, D. N. Sweetnam, and V. R. Eshleman, 1985: The atmosphere of Saturn: An analysis of the Voyager radio occultation measurements. *Astron. J.,* **90,** 1136–1146.

——, J. R. Lyons, and D. N. Sweetnam, 1987: The atmosphere of Uranus: Results of radio occultation measurements with Voyager 2. *J. Geophys. Res.,* **92,** 14 987–15 001.

Lipa, B., and G. L. Tyler, 1979: Statistical and computational uncertainties in atmospheric profiles from radio occultation: Mariner 10 at Venus. *Icarus,* **39,** 192–208.

Marouf, E. A., G. L. Tyler, and V. R. Eshleman, 1982: Theory of radio occultation by Saturn's rings. *Icarus,* **49,** 161–193.

Melbourne, W. G., and Coauthors, 1994: The application of spaceborne GPS to atmospheric limb sounding and global change monitoring. JPL Publication 94-18, 147 pp. [Available from Jet Propulsion Laboratory, 4800 Oak Grove Drive, Pasadena, CA 91109.]

Phinney, R. A., and D. L. Anderson, 1968: On the radio occultation method for studying planetary atmospheres. *J. Geophys. Res.,* **73,** 1819–1827.

Rocken, C., and Coauthors, 1997: Analysis and validation of GPS/MET data in the neutral atmosphere. *J. Geophys. Res.,* **102,** 29 849–29 866.

Smith, E. K., and S. Weintraub, 1953: The constants in the equation for atmospheric refractive index at radio frequencies. *Proc. IRE,* **41,** 1035–1037.

Steffes, P. G., J. M. Jenkins, E. H. Seale, and G. L. Tyler, 1994: Radio occultation studies of the Venus atmosphere with the Magellan spacecraft: 1. Experimental description and performance. *Icarus,* **110,** 71–78.

Thayer, G. D., 1974: An improved equation for the radio refractive index of air. *Radio Sci.,* **9,** 803–807.

Twomey, S., 1977: *Introduction to the Mathematics of Inversion in Remote Sensing and Indirect Measurements.* Elsevier, 243 pp.

Tyler, G. L., 1987: Radio propagation experiments in the outer solar system with Voyager. *Proc. IEEE,* **75,** 1404–1431.

——, E. A. Marouf, R. A. Simpson, H. A. Zebker, and V. R. Eshleman, 1983: The microwave opacity of Saturn's rings at wavelength of 3.6 and 13 cm from Voyager 1 radio occultation. *Icarus,* **54,** 160–188.

——, and Coauthors, 1989: Voyager radio science observations of Neptune and Triton. *Science,* **246,** 1466–1473.

Vorob'ev, V. V., and T. G. Krasil'nikova, 1993: Estimation of the accuracy of the atmospheric refractive index recovery from Doppler shift measurements at frequencies used in the NAVSTAR system. *Phys. Atmos. Ocean,* **29,** 602–609.

Ware, R., 1992: GPS sounding of earth's atmosphere. *GPS World,* **3,** 56–57.

——, and Coauthors, 1996: GPS sounding of the atmosphere from low earth orbit: Preliminary results. *Bull. Amer. Meteor. Soc.,* **77,** 19–40.

Zou, X., Y. H. Kuo, and Y. R. Guo, 1995: Assimilation of atmospheric radio refractivity using a nonhydrostatic adjoint model. *Mon. Wea. Rev.,* **123,** 2229–2249.